Int. J. Electrochem. Sci., 13 **(2018)** 2054 – 2068, doi: 10.20964/2018.02.63

International Journal of
ELECTROCHEMICAL
SCIENCE
www.electrochemsci.org

Hybrid Nanostructures of MoS_2/Sisal Fiber Tubular Carbon as Anode Material for Lithium ion Batteries

Yuanzhou Liu[1], *Aimiao Qin*[1,*], *Shuoping Chen*[1], *Lei Liao*[2,*], *Kaiyou Zhang*[1], *Zilin Mo*[1]

[1] Key Lab New Processing Technology for Nonferrous Metals & Materials Ministry of Education, Guangxi Key Laboratory in Universities of Clean Metallurgy and Comprehensive Utilization for Non-ferrous Metals Resources, College of Materials science & engineering, Guilin University of Technology, Guilin, China
[2]Guangxi Key Laboratory of Environment Pollution Control Theory and Technology, College of Envir onmental Science and Engineering, Guilin University of Technology
Guilin, China
[*]E-mail: 2005032@glut.edu.cn, fangqiu2001@163.com

Received: 17 October 2017 / *Accepted:* 17 December 2017 / *Published:* 28 December 2017

Environmentally friendly and low-cost MoS_2/sisal fiber tubular carbon (MoS_2/SFTC) nanohybrids have been prepared via a facile hydrothermal-anneal strategy, in which the tubular biomass carbon derived from natural sisal fibers as a conductive base. The as-prepared nanohybrids are characterized by Raman spectra, XRD, XPS, FESEM, TEM and EDS. It is shown that the sisal fiber tubular carbons with nanowrinkles and nanofolds were uniformly coated with vertical MoS_2 nanosheets on the surface. As an anode material for lithium ion batteries, the MoS_2/SFTC nanohybrids possess an excellent cycling performance, superior rate capability and high reversible capacity. A reversible specific capacity of 437.2 mA h g^{-1} is maintained after 50 cycles at the current density of 50 mA g^{-1}. Even at a high current density of 2000 mA g^{-1}, the reversible specific capacity could be retained at 241.1 mA h g^{-1}. The superior electrochemical performance of the MoS_2/SFTC nanohybrids can be attributed to the synergistic effects of uniform vertical MoS_2 nanosheets and conductive SFTC nanostructures.

Keywords: Sisal fiber tubular carbon, Hydrothermal-anneal, MoS_2 nanosheets, Nanohybrids, Lithium ion batteries

1. INTRODUCTION

Fabricating device for high-performance and renewable energy storage has great importance for the advancement of electrical vehicles and dire environmental concerns. Rechargeable lithium ion batteries (LIBs) are one promising power for future applications, such as stationary energy storage and electric vehicles, which are crucial to the alleviation of energy crisis and global environmental

concerns [1-3]. Nowadays, graphitic carbons are recognized as the leading electrode material for anodes of commercial LIBs due to its low cost, high electrical conductivity, good chemical stability and long cycling life [4, 5]. Unfortunately, most common graphitic carbons have relatively low theoretical capacity (372 mA h g^{-1}) and poor rate performance cannot meet the urgent requirement of promising power sources with high energy and power densities, such as electric vehicles (EVs) and hybrid EVs (HEVs) [6-8]. Therefore, there is a critical need to develop renewable and advanced anode materials for safe and highly efficient LIBs. Among all available anode materials, biomass carbon (such as rice husk, wheat straw and peanut shells carbons) and transition metal sulfide (such as WS_2, MoS_2 and SnS_2) nanostructure materials have the potential to be used as safe and high performance energy storage materials[9-14].

As is well known, biomass carbons possess a large specific surface area, rich pore structure and good electrical conductivity, these features make them deliver high capacity, favorable rate performance and cycling stability when used as anode materials for LIBs [10]. Meanwhile, as a renewable resource, they have advantages of rich source of raw materials, environment friendly, low cost and easy processing, these characteristics are not available for fossil energy storage materials [15]. However, despite these marvelous features, the use of pure biomass carbons as anodes for LIBs is still hampered by the irreversible capabilities and distinct hysteresis in the voltage profile during charge/discharge cycles [10, 16, 17]. Efforts have been taken to overcome these drawbacks. On the other hand, transition metal sulfides would be the candidates due to their higher theoretical capacity and unusual conversion reaction mechanism [18, 19]. Especially for molybdenum disulfides (MoS_2), they have been suggested as one of promising anode materials for LIBs in view of their high-lithium-storage capacity (ca.670 mA h g^{-1} with 4mol of Li^+ insertion per formula) and low cost [20, 21]. As a typical two-dimensional (2D) transition-metal sulfide, MoS_2 consists of a hexagonally packed layer of Mo atoms sandwiched between two layers of S atoms and the triple layers are stacked and held together by Van der Waals interactions [22, 23]. The weak Van der Waals interactions could provide a convenient environment between the adjacent interlayer for reversibly inserting and extracting abundant lithium ions [21, 24], meanwhile, MoS_2 can also be converted into the metal Mo and LiS_2 with additional lithium storage capacity [25-27]. However, the single layered and/or few layered MoS_2 nanosheets are very easy to stack and restack even in dry process, plus their inherent poor electrical conductivity, greatly inhibiting their potential for application in LIBs [28-30]. To get over these obstacles, one strategy is to hybridize MoS_2 nanosheets with high conductive carbon, which requires that the MoS_2 nanosheets are well maintained and the conductivity is also remarkably improved [31, 32]. Two routes have been developed to obtain such hybrid structures. One is to grow MoS_2 on the surface of carbonaceous materials, e.g., carbon nanotubes [33], graphene [34]; another is to synthesize a MoS_2-C embedded structure [35, 36]. Nevertheless, most of the previous reported methods are complex and expensive, sometimes involving sophisticated techniques, which are hard to scale-up. Therefore, it is essential to develop a method to grow MoS_2 nanosheets on the surface of biomass carbons to achieve a cheaper, more environment friendly and higher electrochemical performance anode material.

Herein, we report a method to directly grow a novel hybrid nanostructure of MoS_2 and sisal fiber tubular carbons (denoted as MoS_2/SFTC) via a facile hydrothermal-annealing method assisted by

ammonium dithiocarbamate ($CH_6N_2S_2$). In the hybrid nanostructures of MoS_2/SFTC, the uniform SFTC were covered with nanowrinkles and nanofolds which have a direction parallel to the direction of the tubular axis, while the 2D MoS_2 nanosheets were vertically grown on the surface of SFTC. When served as an anode material for LIBs, the MoS_2/SFTC nanohybrids show a characterization of higher specific capacity, enhanced cycling stability and better rate capability than that of MoS_2 alone.

2. EXPERIMENTAL SECTION

All the chemical reagents in this study are of analytical grade and are used without further purification. All aqueous solutions are prepared with deionized water.

2.1. Preparation of sisal fiber tubular carbon (SFTC)

Sisal fibers (SFs) were supplied by Guangxi Sisal Group Co., Ltd. The maize-yellow SFs were washed with deionized water to remove the impurities, cut to a length of ~2 cm and dried in the oven at 80 ℃. And then the SFs were treated by a hydrothermal method. 5.0 g of SFs, 70 mL of 2.5 M potassium hydroxide (KOH) solution were placed in a 100-mL Teflon-lined stainless steel autoclave. The mixture solution in the autoclave was first heated to 160 ℃ and kept for 14 h, then cooled down to room temperature. The tawny prepare materials denoted as sisal fiber tubular carbon precursor were collected and washed by deionized water until the pH down to 7, dried in the oven at 80 ℃. Subsequently the dried sisal fiber tubular carbon precursor was put into a nickel crucible, and calcined in a tube furnace at 900 ℃ for 1 h under nitrogen atmosphere with a heating rate of 3 ℃ min^{-1}, after cooled down to room temperature naturally, the black carbonaceous was collected and grinded fully in an agate mortar. The obtained product is denoted as SFTC.

2.2. Syntheses of the MoS_2/SFTC nanohybrids

MoS_2/SFTC nanohybrids were synthesized via a facile hydrothermal-anneal strategy. In a typical reaction, 0.2 g of SFTC and 0.0720 g of MoO_3 were combined with 70 mL of water, after stirred for 15 minutes, 0.1102 g of $CH_6N_2S_2$ was put into the disperse system, and stirred for 20 minutes, then the solution was transferred into a Teflon-lined, 100 mL capacity stainless steel autoclave and kept at 180 ℃ for 36 h. After cooled down to room temperature, the precipitate was isolated and washed three times with deionized water and alcohol, followed by an overnight drying at 80 ℃. Finally, the dried precursor was annealed in a conventional tube furnace at 800 ℃ for 1 h at a heating rate of 3 ℃ min^{-1} in a flowing N2 atmosphere. For comparison, MoS_2 particles without the addition of SFTC are synthesized, in which all other reaction parameters were kept constant.

2.3. Material characterization

The surface morphology and composition of the samples were observed by field-emission scanning electron microscopy (FESEM, S-4800, Hitachi High-Technologies Co.) operated at 5 KV. The compositional analysis and elemental mapping on the as-prepared MoS_2/SFTC nanohybrids were performed with an energy-dispersive X-ray spectroscopy (EDS) system, an accessory of FESEM. Transmission electron microscopy (TEM) measurements were carried out on a JEM-2100F (JEOL) transmission electron microscope, operated at 200 KV accelerating voltage. The crystal structures of the MoS_2/SFTC nanohybrids were characterized by means of powder X-ray diffraction (XRD, X′Pert PRO, PANalytical B.V.), using Cu Kα (λ=1.54056 Å) as radiation source in the 2θ range of 10~80°. Raman spectra of MoS_2 particles and MoS_2/SFTC nanohybrids were obtained at room temperature with a Thermo Fisher Scientific DXR Raman Microscope with the laser excitation of 532 nm. The Mo-related bond features in the synthesized MoS_2/SFTC nanohybrids were identified by X-ray photoelectron spectroscopy measurements (XPS, ESCALAB 250Xi, Thermo Electron Co.), using monochromatic Al Kα (1486.6 eV) as X-ray source.

2.4. Electrochemical measurements

To evaluate the electrochemical performance, coin-type half-cells were assembled using the as-prepared samples as anode materials for lithium-ion batteries. The working electrodes were prepared by mixing the as-synthesized MoS_2/SFTC nanohybrids, SFTC or MoS_2 particles, conductive carbon black, and poly (vinylidene fluoride) binder dispersed in an N-methyl-2-pyrrolidone solution at a weight ratio of 80: 10: 10, respectively. The as-prepared active material slurry was uniformly spread onto Cu foil and dried in a vacuum oven at 110 ℃ for 12 h prior to coincell assembly. The electrochemical experiment were performed using LIR2025-type coin cells, which were assembled in an argon-filled dry glove box (Super 1220/750, Mikrouna) with MoS_2/SFTC nanohybrids or MoS_2 particles as the working electrode, pure lithium foil as the counter and reference electrodes, polypropylene membrane film as the separator, and 1 M $LiPF_6$ in ethylene carbon (EC)-dimethyl carbonate (DMC) as electrolyte. Galvanostatic charging-discharging (GCD) measurements were carried out under different current densities in the voltage range between 0.01 V and 3.0 V on a Neware GCD system. Cyclic voltammetry (CV) was conducted on an electrochemical analyzer (CHI-760D) in the voltage range of 0.01~3.0 V (vs. Li^+/Li) at a scan rate of 0.2 mVs^{-1}. Electrochemical impedance spectroscopy (EIS) was tested on the CHI-760D in the frequency range of 0.01~100 KHz. All electrochemical measurements were performed at room temperature.

3. RESULTS AND DISCUSSION

The preparation process of MoS_2/SFTC nanohybrids is illustrated in Fig. 1. Sisal fibers mainly consist of cellulose, hemicellulose and lignin [37]. Each sisal fiber is composed of a bunch of tubular cellfibre with a multilevel layered structure, the outer surface is a layer of hydrophobic wax, and the

internal layers consist of hundreds of parallel tubular cellfibre, linked by hemicelluloses and lignin [38, 39]. Under a relatively aggressive hydrothermal treatment performed in the KOH solution at 160 ℃, high concentrations of alkali can saponify the wax and dissolve the hemicellulose and lignin, while the tubular cellfibres are partly degraded but not dissolved [10, 40, 41]. After removal of hemicellulose and lignin, the connections between the cellulose fibrils were loosened, the bonded together tubular cellfibres were separated, then rinsed thoroughly, the white tubular cellfibres can be achieved. The obtained tubular cellfibres samples were carbonized at 900 ℃ under a N_2 atmosphere for 1 h, then were cooled down to room temperature and the black tubular carbons can be obtained.

In the subsequent process of MoS_2 nanosheets grown on SFTC directly via a hydrothermal method, a possible formation mechanism is proposed as follows: (i) MoO_3 and SFTC were dispersed in the distilled water firstly and acted as the nanocomposite precursor and base in the following hydrothermal process, respectively. H_2S can be released from subsequent $CH_6N_2S_2$ in a certain temperature, which acts as the sulfur source and reducing agent for the formation of MoS_2 nanosheets [42, 43]. (ii) In the hydrothermal surroundings, MoO_2 crystals were firstly formed [18], then under the synthesis conditions employed by H_2S, they finally converted into MoS_2 nanosheets. Meanwhile, multifunctional groups (-HS,-NH and -SCN) of $CH_6N_2S_2$ can be used for the conjugation of metallic ions to help the growth of nanosheets on the surface of SFTC [44, 45]. After the further annealing treatment at high temperature in a flowing N2 atmosphere, highly crystalline MoS_2/SFTC nanohybrids can be obtained [46].

Figure 1. Schematic illustration of the synthesis procedure of MoS_2/SFTC nanohybrids.

FESEM images show that these tubular cellfibres are highly uniform with an average diameter about 10 μm and fairly long (Fig. 2a); after carbonization, these tubular cellfibres changed into tubular carbons, the diameter reduced to about 3.4 μm, the aperture and wall thickness are about 0.8 μm and 0.6 μm (Fig. 2b). There are many parallel nanowrinkles and nanofolds with thickness about 80 nm on

the surface of SFTC, which possess large amount of hydrophilic functional groups and make these tubular carbons extraordinarily attractive as hard base for the growth of MoS_2 nanosheets.

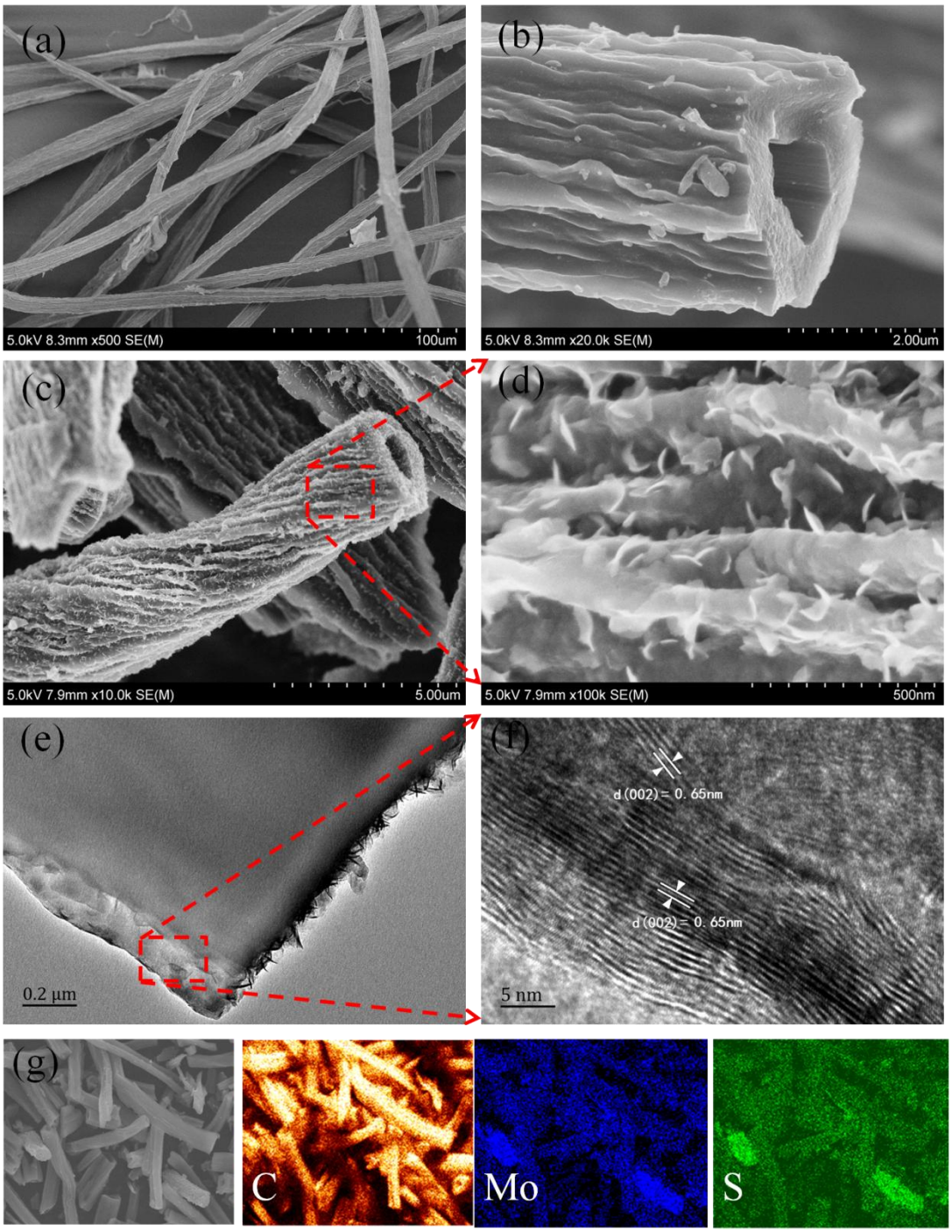

Figure 2. The FESEM images of cellfibres (a), sisal fiber tubular carbon (b) and MoS_2/SFTC nanohybrids (c, d), TEM images of MoS_2/SFTC nanohybrids (e, f), EDS elemental maps of C, Mo and S (g).

Fig. 2c and 2d show typical FESEM images of the MoS_2/SFTC nanohybrids, the low-magnification (Fig. 2c) FESEM image indicates that SFTC is uniformly coated with MoS_2 and the

high-magnification (Fig. 2d) image appears that the MoS_2 show a sheet-like nanostructure with a thickness about 17 nm. It is interesting to note that the growth orientation of MoS_2 nanosheets is vertical to the axis direction of SFTC substrate. The detailed structure of MoS_2/SFTC hybrids was further characterized by TEM as shown in Fig. 2e. In conformity with the above FESEM observations, the low magnification TEM image clearly reveals the hybrid nanostructures of MoS_2/SFTC, it can be observed that the SFTC was served as the base, and the MoS_2 nanosheets were vertically embed into the surface of SFTC. The high-resolution TEM image shows the edge view of some nanosheet structures with visible lattice fringes (Fig. 2f). The interplanar distance was measured to be about 0.65 nm, which is consistent with the d spacing of (002) planes of hexagonal MoS_2 [47]. To illustrate the spatial distribution of MoS_2 and carbon in the MoS_2/SFTC nanohybrids, elemental mapping was performed on a pile of MoS_2/SFTC nanohybrids (Fig. 2g), and the results clearly demonstrate that the elements of C, Mo and S are well distributed within the MoS_2/SFTC nanohybrids.

The crystallographic structure and phase purity of MoS_2/SFTC nanohybrids were examined by XRD. As shown in Fig. 3a, the peaks at 14.12°, 32.91°, 39.51°, 49.41° and 58.76°correspond to (002), (100), (103), (105) and (110) lattice planes of molybdenite (JCPDS no.75-1539), namely 2H-MoS_2. The broad peak at around 24° can be attributed to (002) plane of SFTC. In addition, there are some peaks on 25.99°, 36.92° and 53.45° due to the existence of slightly residual MoO_2, which should be derived from the reduction of MoO_3. Raman spectra were recorded to further reveal the microstructure of the MoS_2 particles and MoS_2/SFTC nanohybrids (Fig. 3b). For MoS_2 particles, the two distinct Raman peaks at 374 and 400 cm^{-1} were ascribed to the typical E^1_{2g} (owing to opposite vibration of two S atoms with respect to Mo atom) and A_{1g} (resulting from the vibration of only S atoms in opposite directions) modes of the hexagonal MoS_2 crystal, respectively [35]. In MoS_2/SFTC nanohybrids, the above two peaks belonging to MoS_2 were shifted to 373 and 401 cm^{-1}. Particularly, the corresponding frequency difference between the E^1_{2g} and A_{1g} mode increased to 28 cm^{-1} compared with 26 cm^{-1} for MoS_2 particles, indicating that the thickness of MoS_2 crystals in the MoS_2/SFTC hybrid nanostructures are slightly increased [48]. The increase of the thickness is reasonable because the SFTC base is very active for the growth of MoS_2 nanosheets.

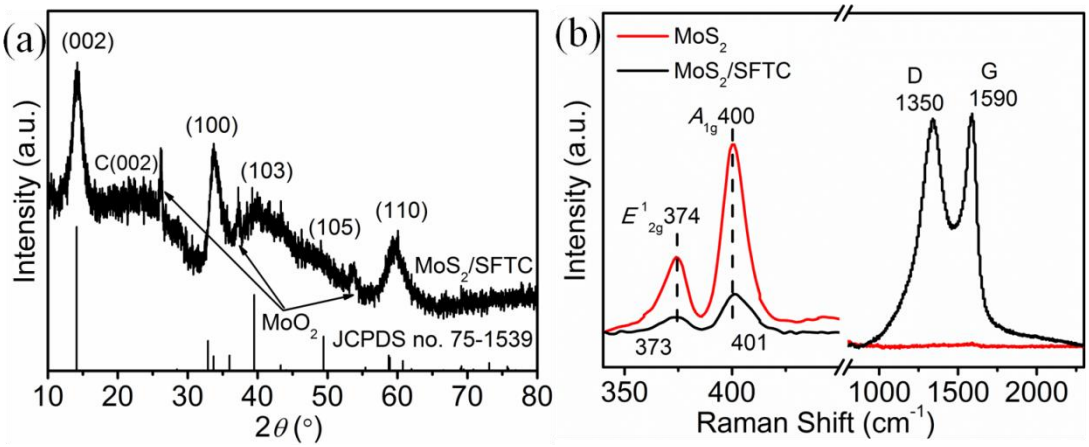

Figure 3. XRD pattern of MoS_2/SFTC nanohybrids (a), Raman spectra of MoS_2 particles and MoS_2/SFTC nanohybrids (b).

As for the carbon-related part in Fig. 3b, the disordered carbon peak (D band) and the ordered graphitic carbon peak (G band) are found at 1350 and 1590 cm^{-1} with the I_D/I_G intensity ratio of ~0.97, implying a relatively high graphitization, which will accelerate electrical conductivity.

To validate the chemical composition and chemical state of the MoS_2/SFTC nanohybrids, the XPS measurements were applied for further investigation and all of the spectra were calibrated by the C1s peak located at 284.8 eV. The survey spectrum measured (Fig. 4a) shows that the MoS_2/SFTC nanohybrids were composed of C, O, Mo and S elements, the peaks of Mo 3d and S 2p can be assigned to the characteristic of MoS_2.

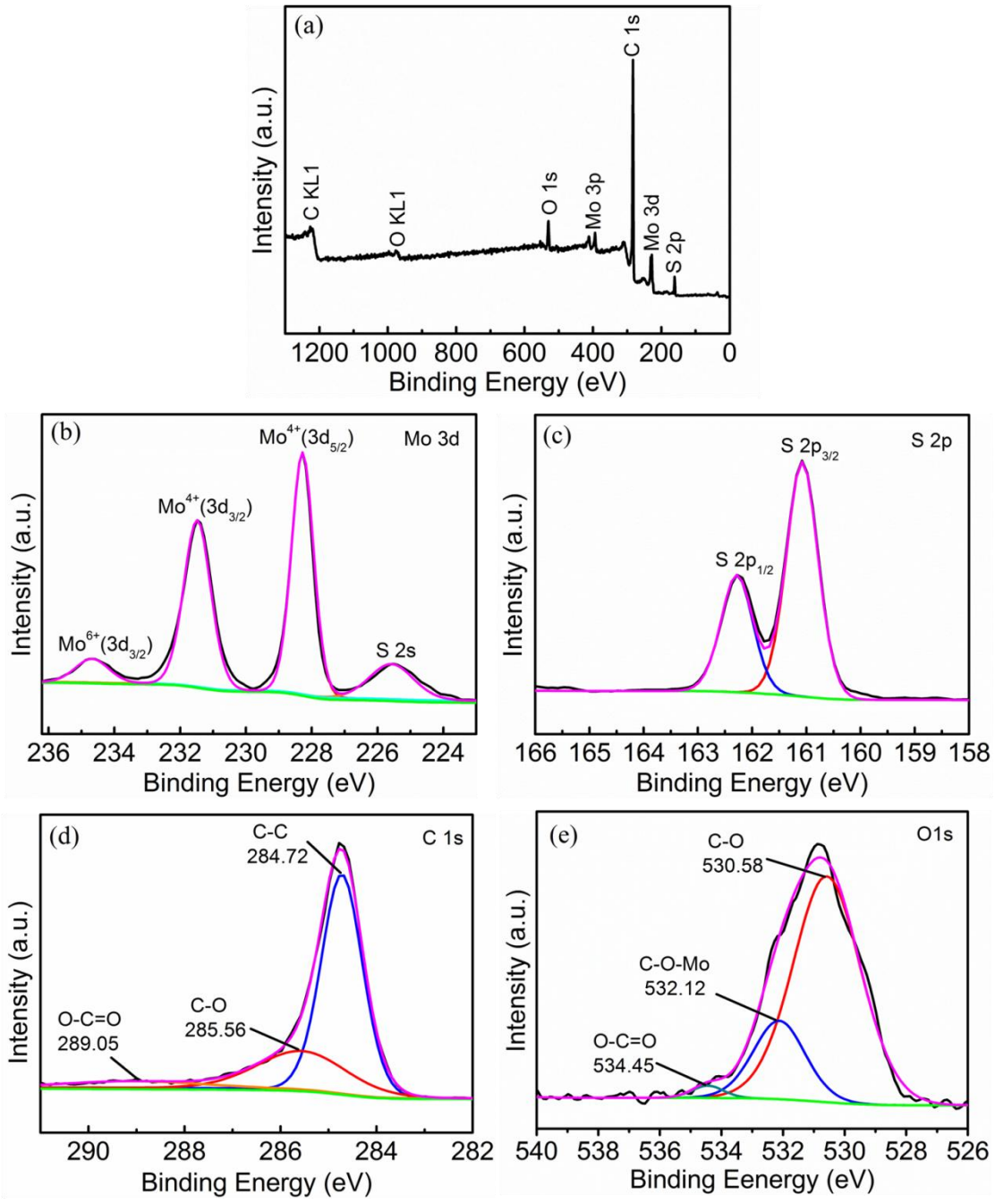

Figure 4. XPS survey spectrum (a), high resolution Mo 3d (b), S 2p (c), C 1s (d), and O 1s (e) spectrum of MoS_2/SFTC nanohybrids.

The Mo 3d peaks were studied by high resolution XPS (Fig. 4b), in which the Mo 3d peak can be fitted into four peaks, the two strong peaks centered at 229.81 and 232.97 eV are attributed to the binding energies of Mo $3d_{5/2}$ and Mo $3d_{3/2}$ of Mo^{4+} respectively, indicating Mo (Ⅳ) oxidation state in agreement with previous reports [49, 50]. Additionally, the peak at 236.09 eV is related to the Mo $3d_{3/2}$ of Mo^{6+} (typical of the Mo-O bond) [51]. Another small peak at 226.98 eV corresponds to the S 2s component. For the high resolution spectrum of S 2p (Fig. 4c), the two peaks located at 161.07 and 162.26 eV arise from the binding energies S $2p_{3/2}$ and S $2p_{1/2}$ orbital of divalent sulfide ions (S^{2-}) [18]. The C 1s high resolution spectrum (Fig. 4d) consists of three types of carbon species, with the strong peak 284.72 eV assigned to the C-C bonds in the carbon base, while the weak ones C-O at 285.56 eV, C=O at 289.05 eV. Notably, the high resolution spectrum of O 1s (Fig. 4e) can be deconvoluted into three peaks, in which there is a new peak at 532.12 eV, apart from the one at 530.58 eV for C-O, and another at 534.45 eV for O-C=O. It is reported that the O1s peak in the C-O-metal bond is located at ca. 530 ~ 533 eV, and this bond can enhance the electron transport rate and structural stability of hybrid nanostructures [52, 53]. Therefore, we can conclude that the C-O-Mo bonds are form in the MoS_2/SFTC hybrid nanostructures, and they should be beneficial for the improvement of electrochemical performance.

To identify electrochemical behavior versus Li for the MoS_2/SFTC nanohybrids electrode, cyclic voltammetry (CV) of the half-cell was performed in the range from 0.01 to 3.0 V at a scanning rate of 0.2 mVs^{-1} (Fig. 5a). In the first cathodic scan, the reduction peak at around 2.04 V is observed, it is likely to be related to the formation of Li_2S [21]; the other reduction peak is found at 1.07 V, due to the intercalation of Li^+ ions on different defect sites of MoS_2 and the formation of Li_xMoS_2 according to eqn (1) [18]; and the pronounced peak located at 0.43 V can be ascribed to the reduction of Li_xMoS_2 to Mo metal and Li_2S according to eqn (2) [54]; meanwhile the two weak reduction peak at around 1.62 V and 1.25 V can be attributed to the formation of Li_xMoO_2 ($MoO_2 + xLi^+ + xe^- \rightarrow Li_xMoO_2$) [55]. In the reverse anodic scan, two weak peaks at 1.45 and 1.75 V can be put down to the delithiation of Li_xMoO_2 [56]; the broad peak at 2.30 V is assigned to delithiation of Li_2S according to eqn (3) [57]. In the subsequent cathodic scan, the reduction peaks at 2.04, 1.07 and 0.43 V disappeared due to the formation of a solid electrolyte interface (SEI) layer at the interface of electrolyte and electrode (a polymer/ gel-like film) [35, 58], and three new reduction peaks at around 1.97, 0.90 and 0.4 V emerged, the 1.97 V is indicative of the formation of Li_2S, the 0.9 and 0.4 V are attributed to the association of Li with Mo[59]. Other three new weak reduction peaks at around 1.60, 1.40 and 1.30 V are owing to the phase transformation between the MoO_2 and Li_xMoO_2 during the insertion [60]. Furthermore, there is a reversible redox couple located at 0.02/0.43 V, which could be ascribed to the phase transformation of carbon in SFTC to Li_xC_6 according to eqn (4) [56], indicating that the SFTC matrixes are electrochemically active for lithiation/delithiation. Additionally, the change of the position of redox peaks is not observed in subsequent cycles indicating the high reversibility of phase transitions. The high reversibility is mainly attributed to the stable hybridization structures of the electrode.

$$MoS_2 + xLi^+ + xe^- \rightarrow Li_xMoS_2 \quad (1)$$

$$Li_xMoS_2 + (4 - x)\,Li^+ + (4 - x)\,e^- \rightarrow Mo + 2Li_2S \quad (2)$$

$$Li_2S \rightarrow S + 2Li^+ + 2e^- \quad (3)$$

$$6C + xLi \rightarrow Li_xC_6 \quad (4)$$

Fig. 5b shows the initial three charge and discharge curves of the MoS_2/SFTC nanohybrids electrode measured at a current density of 50 mA g^{-1} between 0.01 and 3.0 V. At the first discharge/charge cycle, the discharge and charge capacities are 907.8 and 448.3 mA h g^{-1}, respectively, with an initial Coulombic efficiency of 49.4%, the high capacity at the first discharge can be attributed to the irreversible capacity arising from SEI formation which is coupled with the decomposition of electrolyte. In the subsequent discharge/charge processes, the capacity maintained at 456.6 and 407.7 mA h g^{-1} respectively, the Coulombic efficiency increased to about 89.2%. In the third discharge/charge processes, the capacity retained about 426.5 and 398.2 mA h g^{-1}, the Coulombic efficiency changed to 93.3%. Furthermore, all plateaus are in good agreement with the CV results, indicating that the discharge/charge electrochemical behaviors of MoS_2/SFTC nanohybrids electrode were almost consistent with CV measurements results [61, 62].

To study the stability of electrode, discharge/charge cycling performance was evaluated between 0.01 and 3.0 V at a current density of 50 mA g^{-1} for 50 cycles, as shown in Fig. 5c. As was expected, MoS_2/SFTC nanohybrids electrode possess an enhanced cycling stability compared with MoS_2-based anode material. From the second cycle onwards, MoS_2/SFTC nanohybrids electrode showed an excellent cycling stability with little fading of capacity over the first 50 cycles, and a high reversible capacity of 437.2 mA h g^{-1} was still maintained after 50 cycles, the cycling and capacity performance even as good as the performance of MoS_2/graphene[63] and MoS_2/carbon nanotube[64] that have reported. Under the identical test conditions, the MoS_2 particles afforded a reversible capacity of 660.7 mA h g^{-1} at the first cycle, which is approximate the theoretical one, but the reversible capacity exhibited faster fading than that of MoS_2/SFTC nanohybrids electrode at the following cycles, there was only around 80 mA h g^{-1} retained after 50 cycles. For further comparison, the cycle performance of SFTC electrode is also shown in Fig. 5c. It can be seen that the cycle stability of SFTC is great, while the reversible capacity only remained 229.9 mA h g^{-1} at 50 mA g^{-1} after 50 cycles. Hence, the advantage of MoS_2/SFTC nanohybrids for lithium storage is quite apparent.

In order to evaluate the rate capability, the MoS_2/SFTC nanohybrids electrode was cycled at various charge/discharge current densities range from 50 to 2000 mA g^{-1} over a voltage window of 0.01~3.0 V (Fig. 5d). As shown in Fig. 5d, with the increase of charge/discharge current densities from 50 to 2000 mA g^{-1}, the reversible capacities are ca. 424.6, 384.7, 360.0, 325.7, 297.5, and 241.1 mA h g^{-1} at current densities 50, 100, 200, 500, 1000, and 2000 mA g^{-1}, respectively. When the current density dropped back to 50 mA g^{-1}, the specific capacity of the hybrids was recovered to 456.56 mA h g^{-1}, implying the highly stable cycling performance and good reversibility. The excellent cycling stability and high rate performance of this MoS_2/SFTC nanohybrids could be attributed to the rational design and engineering of the unique nanostructure and composition. Especially, the sheet-like nanostructures possess a shorter distance for Li^+ diffusion and larger electrode-electrolyte contact area for high Li^+ flux across the interface, resulting in the enhanced rate capability [65, 66]. Moreover, in the microstructure of MoS_2/SFTC nanohybrids, the tubular carbon provides a good supporting matrix to maintain the structural integrity, also affords an elasticity to alleviate the volume change and good conductivity during cycling. Particularly, the C-O-Mo bonds could supply a continuous pathway for

electron transport and prevent the MoS_2 nanosheets fall off during the electrochemical processes [46, 67].

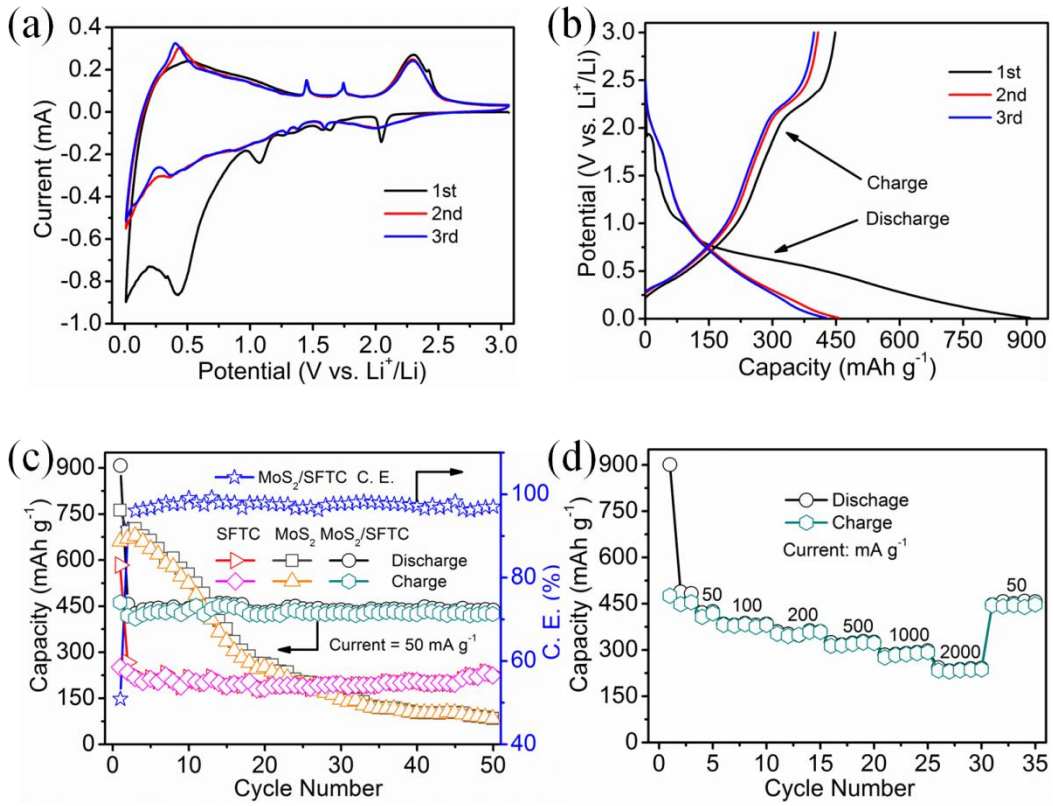

Figure 5. CV curves at a scan rate of 0.2 mVs^{-1} (a) and charge/discharge curves at a current density of 50 mA g^{-1} for the initial 3 cycles of the MoS_2/SFTC nanohybrids electrode (b), cycling behavior and columbic efficiency of the MoS_2/SFTC nanohybrids electrode, and cycling performance of the SFTC and MoS_2 particles electrodes at a current density of 50 mA g^{-1}(c), rate capabilities of the MoS_2/SFTC nanohybrids electrode (d).

In order to a better understand of the surface-dependent LIB performance, EIS measurements were taken for MoS_2, SFTC and MoS_2/SFTC nanohybrids electrodes before discharge/charge cycle (Fig. 6a), and the simplified equivalent circuit was use to interpret the measured results (Fig. 6b). As shown in Fig. 6a, all these plots consist of two parts: a semicircle which is relate to the electrolyte resistance (*R*s) and charge transfer resistance (*R*ct) at high frequencies, a short inclined line relating to the ion diffusion (*Z*w) and constant phase element (CPE) in low frequency regions within the anode [48, 56]. The semicircle for MoS_2/SFTC nanohybrids electrode was much smaller than that of MoS_2, indicating that the SFTC base can facilitate electron transfer and thus decrease resistance. The *R*ct is a key indicator for the kinetics of the electrode material [68]. Table 1 lists the parameters of the equivalent circuit for MoS_2, SFTC and MoS_2/SFTC nanohybrids electrodes after fitted the diameter of the semi-circular curve. Evidently, the *R*ct of MoS_2/SFTC nanohybrids electrode was much smaller than that of MoS_2 particles electrode, suggesting that the electron transference of the former is better than the latter.

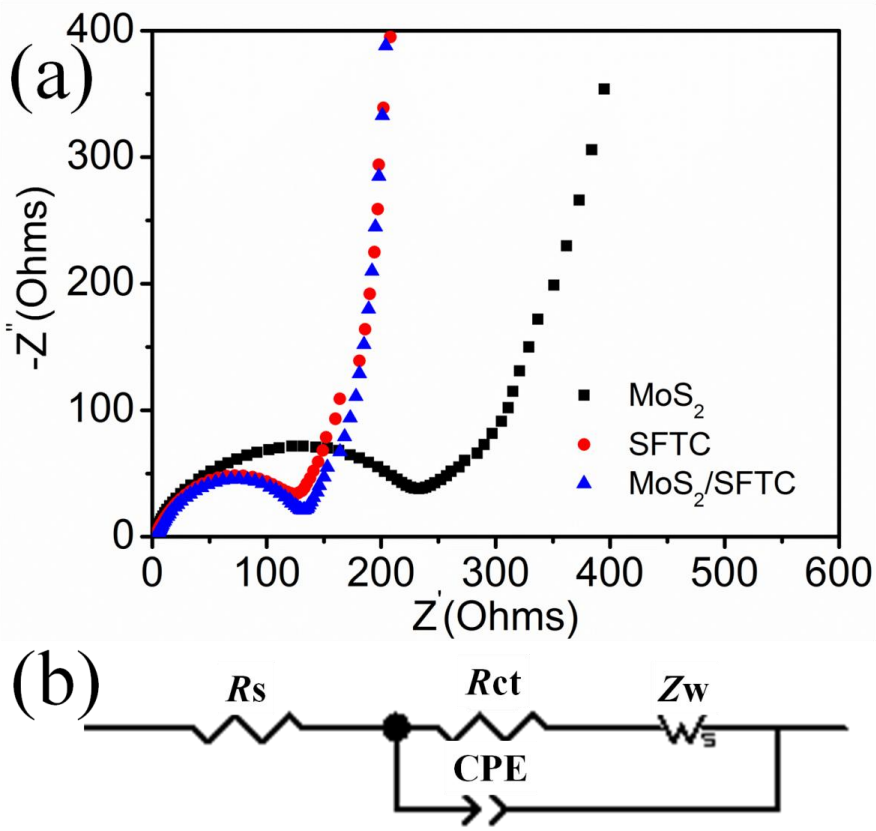

Figure 6. Electrochemical impedance spectra (EIS) of MoS_2, SFTC and MoS_2/SFTC nanohybrids electrodes in the frequency range from 0.01~100 kHz (a), Equivalent circuit model (b).

Table 1. Impedance parameters calculated from an equivalent circuit model

Samples	*Rs* (Ω)	*Rct* (Ω)
MoS_2	1.087	216.0
SFTC	3.137	124.9
MoS_2/SFTC	2.358	119.7

4. CONCLUSIONS

In summary, we have successfully fabricated the MoS_2/SFTC nanohybrids through a facile hydrothermal-anneal strategy, with the natural sisal fibers as the carbon precursor. In the hybrid nanostructures, the tubular carbon matrix with nanowrinkles and nanofolds is evenly covered with MoS_2 nanosheets, the nanosheets have a growth orientation vertical to the axis direction of SFTC. As an anode material for LIBs, the MoS_2/SFTC nanohybrids show a better electrochemical performance than that of MoS_2 particles alone. The excellent electrochemical performances of MoS_2/SFTC nanohybrids are attributed to their unique hybrid nanostructures where the MoS_2 nanosheets and the tubular carbon base created a synergistic effect. Moreover, sisal fibers, a common polymer derived

from biomass, act as the carbon source, which makes the facile synthesis process environmentally friendly and sustainably.

ACKNOWLEDGEMENTS
This work was financially supported by the National Natural Science Foundation of China (No.51564009, 51468011), the Natural Science Foundation of Guangxi (No.2015GXNSFDA139035), and the Research Funds of Guangxi Experiment Center of Information Science (No. KF1407).

References

1. J. Hou, C. Cao, F. Idrees, X. Ma, *ACS Nano*, 9 (2015) 2556-2564.
2. P. Simon, Y. Gogotsi, *Nat. Mater.*, 7 (2008) 845-854.
3. C.M.A. Parlett, K. Wilson, A.F. Lee, *Chem. Soc. Rev.*, 42 (2013) 3876-3893.
4. J.P. Marco-Lozar, M. Kunowsky, F. Suarez-Garcia, J.D. Carruthers, A. Linares-Solano, *Energy Environ. Sci.*, 5 (2012) 9833-9842.
5. J. Jiang, J. Zhu, W. Ai, Z. Fan, X. Shen, C. Zou, J. Liu, H. Zhang, T. Yu, *Energy Environ. Sci.*, 7 (2014) 2670-2679.
6. Y. Zhai, Y. Dou, D. Zhao, P.F. Fulvio, R.T. Mayes, S. Dai, *Adv. Mater.*, 23 (2011) 4828-4850.
7. Y. Li, Z.-Y. Fu, B.-L. Su, *Adv. Funct. Mater.*, 22 (2012) 4634-4667.
8. X. Yang, C. Cheng, Y. Wang, L. Qiu, D. Li, *Science*, 341 (2013) 534-537.
9. Y. Shen, *J. Agric. Food Chem.*, 65 (2017) 995-1004.
10. X. Zhou, F. Chen, T. Bai, B. Long, Q. Liao, Y. Ren, J. Yang, *Green Chem.*, 18 (2016) 2078-2088.
11. W. Lv, F. Wen, J. Xiang, J. Zhao, L. Li, L. Wang, Z. Liu, Y. Tian, *Electrochim. Acta*, 176 (2015) 533-541.
12. S. Liu, B. Shen, Y. Niu, M. Xu, *J. Colloid Interface Sci.*, 488 (2017) 20-25.
13. D. Wang, Y. Xiao, X. Luo, Z. Wu, Y.-J. Wang, B. Fang, *ACS Sustain. Chem. Eng.*, 5 (2017) 2509-2515.
14. J. Zai, K. Wang, Y. Su, X. Qian, J. Chen, *J. Power Sources*, 196 (2011) 3650-3654.
15. L. Chen, Y. Zhang, C. Lin, W. Yang, Y. Meng, Y. Guo, M. Li, D. Xiao, *J. Mater. Chem. A*, 2 (2014) 9684-9690.
16. Y. Fang, Y. Lv, R. Che, H. Wu, X. Zhang, D. Gu, G. Zheng, D. Zhao, *J. Am. Chem. Soc.*, 135 (2013) 1524-1530.
17. C. Hu, L. Wang, Y. Zhao, M. Ye, Q. Chen, Z. Feng, L. Qu, *Nanoscale*, 6 (2014) 8002-8009.
18. S. Hu, W. Chen, J. Zhou, F. Yin, E. Uchaker, Q. Zhang, G. Cao, *J. Mater. Chem. A*, 2 (2014) 7862-7872.
19. C. George, A.J. Morris, M.H. Modarres, M. De Volder, *Chem. Mater.*, 28 (2016) 7304-7310.
20. L. Wang, Z. Xu, W. Wang, X. Bai, *J. Am. Chem. Soc.*, 136 (2014) 6693-6697.
21. T. Stephenson, Z. Li, B. Olsen, D. Mitlin, *Energy Environ. Sci.*, 7 (2014) 209-231.
22. C. Lee, H. Yan, L.E. Brus, T.F. Heinz, J. Hone, S. Ryu, *Acs Nano*, 4 (2010) 2695-2700.
23. J.N. Coleman, M. Lotya, A. O'Neill, S.D. Bergin, P.J. King, U. Khan, K. Young, A. Gaucher, S. De, R.J. Smith, I.V. Shvets, S.K. Arora, G. Stanton, H.-Y. Kim, K. Lee, G.T. Kim, G.S. Duesberg, T. Hallam, J.J. Boland, J.J. Wang, J.F. Donegan, J.C. Grunlan, G. Moriarty, A. Shmeliov, R.J. Nicholls, J.M. Perkins, E.M. Grieveson, K. Theuwissen, D.W. McComb, P.D. Nellist, V. Nicolosi, *Science*, 331 (2011) 568-571.
24. J. Xiao, D. Choi, L. Cosimbescu, P. Koech, J. Liu, J.P. Lemmon, *Chem. Mater.*, 22 (2010) 4522-4524.
25. M. Chhowalla, H.S. Shin, G. Eda, L.-J. Li, K.P. Loh, H. Zhang, *Nat. Chem.*, 5 (2013) 263-275.
26. L. David, R. Bhandavat, G. Singh, *Acs Nano*, 8 (2014) 1759-1770.

27. H. Liu, D. Su, R. Zhou, B. Sun, G. Wang, S.Z. Qiao, *Adv. Energy Mater.*, 2 (2012) 970-975.
28. K. Chang, W. Chen, *J. Mater. Chem.*, 21 (2011) 17175-17184.
29. C. Feng, J. Ma, H. Li, R. Zeng, Z. Guo, H. Liu, *Mater. Res. Bull.*, 44 (2009) 1811-1815.
30. Z. Wang, T. Chen, W. Chen, K. Chang, L. Ma, G. Huang, D. Chen, J.Y. Lee, *J. Mater. Chem. A*, 1 (2013) 2202-2210.
31. D. Ren, Y. Hu, H. Jiang, Z. Deng, P. Saha, H. Jiang, C. Li, *ACS Sustain. Chem. Eng.*, 4 (2016) 1148-1153.
32. L. Ma, J. Ye, W. Chen, D. Chen, J.Y. Lee, *Nano Energy*, 10 (2014) 144-152.
33. J. Guo, X. Chen, S. Jin, M. Zhang, C. Liang, *Catal. Today*, 246 (2015) 165-171.
34. D. Ren, H. Jiang, Y. Hu, L. Zhang, C. Li, *RSC Adv.*, 4 (2014) 40368-40372.
35. C. Cui, X. Li, Z. Hu, J. Xu, H. Liu, J. Ma, *RSC Adv.*, 5 (2015) 92506-92514.
36. J. Wang, J. Liu, D. Chao, J. Yan, J. Lin, Z.X. Shen, *Adv. Mater.*, 26 (2014) 7162-7169.
37. Z. Yang, H. Guo, X. Li, Z. Wang, Z. Yan, Y. Wang, *J. Power Sources*, 329 (2016) 339-346.
38. P.S. Mukherjee, K.G. Satyanarayana, *J. Mater. Sci.*, 19 (1984) 3925-3934.
39. E.T.N. Bisanda, M.P. Ansell, *J. Mater. Sci.*, 27 (1992) 1690-1700.
40. N. Reddy, Y. Yang, *J. Agric. Food Chem.*, 55 (2007) 8570-8575.
41. R. Liu, H. Yu, Y. Huang, *Cellulose*, 12 (2005) 25-34.
42. D.C. Menezes, G.M. de Lima, A.O. Porto, C.L. Donnici, J.D. Ardisson, A.C. Doriguetto, J. Ellena, *Polyhedron*, 23 (2004) 2103-2109.
43. S. Zhang, B.V.R. Chowdari, Z. Wen, J. Jin, J. Yang, *Acs Nano*, 9 (2015) 12464-12472.
44. F. Sun, Y. Wei, J. Chen, D. Long, L. Ling, Y. Li, J. Shi, *Nanoscale*, 7 (2015) 13043-13050.
45. L. Zhang, X.W. Lou, *Chem.–Eur. J.*, 20 (2014) 5219-5223.
46. H. Jiang, D. Ren, H. Wang, Y. Hu, S. Guo, H. Yuan, P. Hu, L. Zhang, C. Li, *Adv. Mater.*, 27 (2015) 3687-3695.
47. P. Cheng, K. Sun, Y.H. Hu, *RSC Adv.*, 6 (2016) 65691-65697.
48. T.-T. Shan, S. Xin, Y. You, H.-P. Cong, S.-H. Yu, A. Manthiram, *Angew. Chem. Int. Ed.*, 55 (2016) 12783-12788.
49. Y. Sun, X. Hu, W. Luo, Y. Huang, *ACS Nano*, 5 (2011) 7100-7107.
50. J.G. Choi, L.T. Thompson, *Appl. Surf. Sci.*, 93 (1996) 143-149.
51. Y. Sun, X. Hu, W. Luo, Y. Huang, *J. Mater. Chem.*, 22 (2012) 425-431.
52. Y. Teng, H. Zhao, Z. Zhang, Z. Li, Q. Xia, Y. Zhang, L. Zhao, X. Du, Z. Du, P. Lv, K. Świerczek, *ACS Nano*, 10 (2016) 8526-8535.
53. J. Zhou, J. Li, K. Liu, L. Lan, H. Song, X. Chen, *J. Mater. Chem. A*, 2 (2014) 20706-20713.
54. D. Ren, Y. Hu, H. Jiang, Z. Deng, S. Petr, H. Jiang, C. Li, *ACS Sustain. Chem. Eng.*, 4 (2016) 1148-1153.
55. S. Tang, B. Ouyang, L. Yang, W. Ji, *RSC Adv.*, 5 (2015) 50705-50710.
56. Z.X. Huang, Y. Wang, Y.G. Zhu, Y. Shi, J.I. Wong, H.Y. Yang, *Nanoscale*, 6 (2014) 9839-9845.
57. B. Chen, N. Zhao, L. Guo, F. He, C. Shi, C. He, J. Li, E. Liu, *Nanoscale*, 7 (2015) 12895-12905.
58. D.K. Nandi, U.K. Sen, D. Choudhury, S. Mitra, S.K. Sarkar, *Electrochim. Acta*, 146 (2014) 706-713.
59. K. Chang, D. Geng, X. Li, J. Yang, Y. Tang, M. Cai, R. Li, X. Sun, *Adv. Energy Mater.*, 3 (2013) 839-844.
60. K. Palanisamy, Y. Kim, H. Kim, J.M. Kim, W.-S. Yoon, *J. Power Sources*, 275 (2015) 351-361.
61. Q. Wang, J. Li, *J. Phys. Chem. C*, 111 (2007) 1675-1682.
62. J. Xiao, X. Wang, X.-Q. Yang, S. Xun, G. Liu, P.K. Koech, J. Liu, J.P. Lemmon, *Adv. Funct. Mater.*, 21 (2011) 2840-2846.
63. H. Liu, X. Chen, L. Deng, X. Su, K. Guo, Z. Zhu, *Electrochim. Acta*, 206 (2016) 184-191.
64. S.K. Das, *Mater. Lett.*, 130 (2014) 240-244.
65. X. Cui, X. Chen, S. Chen, F. Jia, S. Yang, Z. Lin, Z. Shi, H. Deng, *J. Alloys Compd.*, 693 (2017) 955-963.

66. B. Zhao, Z. Wang, Y. Gao, L. Chen, M. Lu, Z. Jiao, Y. Jiang, Y. Ding, L. Cheng, *Appl. Surf. Sci.*, 390 (2016) 209-215.
67. D. Kong, H. He, Q. Song, B. Wang, W. Lv, Q.-H. Yang, L. Zhi, *Energy Environ. Sci.*, 7 (2014) 3320-3325.
68. R. Wang, C. Xu, J. Sun, Y. Liu, L. Gao, H. Yao, C. Lin, *Nano Energy*, 8 (2014) 183-195